ACS APPLIED MATERIALS & INTERFACES

Research Article

Cite This: ACS Appl. Mater. Interfaces 2018, 10, 4921−4928

www.acsami.org

Effect of Metal Doping and Vacancies on the Thermal Conductivity of Monolayer Molybdenum Diselenide

Milad Yarali,[†,⊥] Hatem Brahmi,[†,⊥] Zhequan Yan,[§] Xufan Li,[∥] Lixin Xie,[‡] Shuo Chen,[‡] Satish Kumar,[§] Mina Yoon,[∥] Kai Xiao,[∥] and Anastassios Mavrokefalos*[,†]

[†]Department of Mechanical Engineering and [‡]Department of Physics and TcSUH, University of Houston, Houston, Texas 77204, United States

[§]G.W. Woodruff School of Mechanical Engineering, Georgia Institute of Technology, Atlanta, Georgia 30313, United States

[∥]Center for Nanophase Materials Sciences, Oak Ridge National Laboratory, Oak Ridge, Tennessee 37830, United States

Supporting Information

ABSTRACT: It is well understood that defect engineering can give rise to exotic electronic properties in transition-metal dichalcogenides, but to this date, there is no detailed study to illustrate how defects can be engineered to tailor their thermal properties. Here, through combined experimental and theoretical approaches based on the first-principles density functional theory and Boltzmann transport equations, we have explored the effect of lattice vacancies and substitutional tungsten (W) doping on the thermal transport of the suspended molybdenum diselenide ($MoSe_2$) monolayers grown by chemical vapor deposition (CVD). The results show that even though the isoelectronic substitution of the W atoms for Mo atoms in CVD-grown $Mo_{0.82}W_{018}Se_2$ monolayers reduces the Se vacancy concentration by 50% compared to that found in the $MoSe_2$ monolayers, the thermal conductivity remains intact in a wide temperature range. On the other hand, Se vacancies have a detrimental effect for both samples and more so in the $Mo_{0.82}W_{018}Se_2$ monolayers, which results in thermal conductivity reduction up to 72% for a vacancy concentration of 4%. This is because the mass of the W atom is larger than that of the Mo atom, and missing a Se atom at a vacancy site results in a larger mass difference and therefore kinetic energy and potential energy difference. Furthermore, the monotonically increasing thermal conductivity with temperature for both systems at low temperatures indicates the importance of boundary scattering over defects and phonon−phonon scattering at these temperatures.

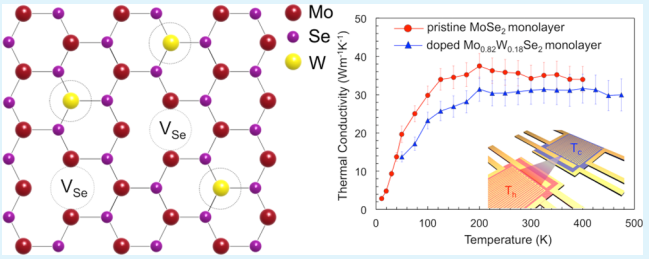

KEYWORDS: *thermal conductivity, transition-metal dichalcogenides, molybdenum diselenide, defect engineering, vacancy, isoelectronic doping*

INTRODUCTION

The unique electronic and optoelectronic characteristics of two-dimensional (2D) transition-metal dichalcogenides (TMDs), notably MoS_2 and $MoSe_2$, classify them as graphene alternatives with regard to fundamental science and technological implications. These layered materials exhibit promising properties, such as indirect-to-direct bandgap crossover in the visible spectrum,[1,2] highly efficient photovoltaic response,[3] strong photoluminescence (PL),[4−6] optically controllable valley polarization[7] as well as field-induced transport with high on−off ratios.[8] In addition, they have recently appeared in the horizon of thermoelectric applications, thanks to their large and tunable Seebeck coefficient.[9−11] To achieve high quality for such layered materials, various techniques[12−15] have been adopted among which molecular beam epitaxy[16] and chemical vapor deposition (CVD)[17] are more desirable because of their scalability for industrial device fabrication. However, because of the imperfection of growth processes, the monolayer TMDs synthesized by these techniques contain higher density of unintentional localized defects, such as vacancies, dislocation cores, and grain boundaries, compared with mechanically exfoliated ones from bulk crystal.[18−24] Recently, isoelectronic doping has been shown to be an effective strategy to suppress the vacancy concentration, enable faster quenching of defect-related emissions by raising the energy of deep level defects, enhance photoluminescence (PL) accompanied by a longer excitation lifetime, as well as modulate the carrier type in CVD-grown $MoSe_2$ monolayer.[23,25,26]

Beyond exploring the electron transport characteristics, deep understanding and manipulation of the phonon transport properties in 2D TMDs is crucial for their successful technological integration, specifically for heat management and hot spot minimization in high-performance solid-state electronic and optoelectronic devices as well as lattice thermal conductivity reduction for enhancing thermoelectric energy conversion efficiency (figure of merit). From the discovery of graphene,[27−29]

Received: September 20, 2017
Accepted: January 11, 2018
Published: January 11, 2018

DOI: 10.1021/acsami.7b14310
ACS Appl. Mater. Interfaces 2018, 10, 4921−4928

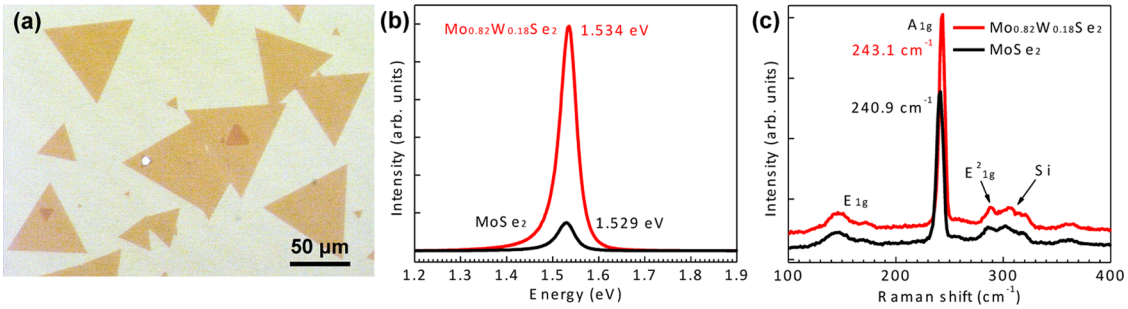

Figure 1. $MoSe_2$ and $Mo_{1-x}W_xSe_2$ monolayers. (a) Optical micrograph of monolayer $MoSe_2$ grown on a SiO_2/Si substrate. (b) PL spectra of monolayer $MoSe_2$ (black curve) and $Mo_{0.82}W_{0.18}Se_2$ (red curve) using 532 nm laser excitation. (c) Raman spectra of monolayer $MoSe_2$ (black curve) and $Mo_{0.82}W_{0.18}Se_2$ (red curve) using 532 nm laser excitation. The Raman spectra were offset for clarity.

which is composed of only one atomic layer of carbon, intensive investigations have been carried out to explore its heat conducting capability and the topic has been of a great interest for both fundamental science[30−33] and practical relevance.[34] On the other hand, to this date, only a limited number of experimental data exists in the literature on the thermal transport for monolayer 2D TMDs due mostly to increased complexity from the involved binary element system and experimental challenges in sample preparation and measurements. Recently, by utilizing micro-Raman thermometry, room-temperature thermal conductivity of 34.5 ± 4,[35] 62.2,[36] and 84 ± 17 W m^{-1} K^{-1}[37] was measured for MoS_2 and 59 ± 18 W m^{-1} K^{-1}[37] for $MoSe_2$ monolayer flakes exfoliated from bulk crystal. Compared with experimental works, there is an increasing number of investigations based on theoretical[38−40] and computational[41] predictions in which room-temperature thermal conductivity of defect-free monolayer MoS_2 and $MoSe_2$ has been reported to be 83−155 and 41−54 W m^{-1} K^{-1}, respectively. Furthermore, it has been recently predicted that vacancies can suppress the thermal conductivity of MoS_2 monolayer.[40,42] To shed light on the kind of nanostructured features required to tailor the transport properties and eventually enable the realization of the transformative potential of 2D TMDs for desired applications, it is paramount to unlock the causal relationship between the perturbations in the lattice arrangement and the phonon characteristics in this promising layered material system.

Here, we employed a suspended microdevice[43,44] on the basis of resistance thermometry to probe the temperature-dependent and intrinsic basal plane thermal conductivity of the pristine $MoSe_2$ and isoelectronic W-substituted $Mo_{1-x}W_xSe_2$ monolayers synthesized by the CVD method. Experimental results reveal that even though substitutional W doping significantly suppresses the Se vacancy concentration in the $Mo_{0.82}W_{018}Se_2$ monolayer, its thermal conductivity remains intact. Our theoretical model is based on the first-principles density functional theory (DFT) and Boltzmann transport equations (BTEs) for quantitatively interpreting the experimental data and specifically for elucidating the influence of Se vacancies on the thermal conductivity of monolayer $MoSe_2$. Our results deepen our fundamental understanding of the underlying phonon transport mechanism in 2D TMDs and throw light on the overall possibility and scope of implementation of these promising atomically thin semiconductors as graphene alternatives.

EXPERIMENTAL SECTION

Material Synthesis and Characterization. The $MoSe_2$ and $Mo_{1-x}W_xSe_2$ monolayers were grown on SiO_2/Si substrates using the CVD method, as reported previously,[23,25,26] in which Se powder was evaporated to react with MoO_3 or mixture of MoO_3 and WO_3 in the presence of hydrogen gas. In this study, we choose $Mo_{1-x}W_xSe_2$ with a typical W concentration (x = 0.18, i.e., $Mo_{0.82}W_{0.18}Se_2$), as quantified in ref 23. The as-grown $MoSe_2$ and $Mo_{0.82}W_{0.18}Se_2$ monolayers show a similar triangular shape (with occasional bilayer islands), with typical lateral sizes between ∼50 and 80 μm (Figure 1a). PL (Figure 1b) and Raman (Figure 1c) spectra are evidence for monolayer $MoSe_2$ and $Mo_{0.82}W_{0.18}Se_2$ (ref 26). As shown in Figure 1b, the PL intensity is greatly (by ∼10 times) enhanced in $Mo_{0.82}W_{0.18}Se_2$ monolayers due to suppression of Se vacancies (by ∼50%) as a result of isoelectronic W substitution.[23] The Raman spectra indicate slight phonon hardening of $Mo_{0.82}W_{0.18}Se_2$ monolayers with little blueshift (by 2.2 cm^{-1}) of the A_{1g} vibration mode (Figure 1c).

Thermal Measurements. The suspended microdevice used to perform thermal transport measurements is shown in Figure 2a−c. The heart of the microdevice is two adjacent membranes made by low-stress silicon nitride (SiN_x). Each of these membranes was suspended by six long SiN_x beams over a through-substrate hole. A serpentine platinum (Pt) line that serves as a heater and resistance thermometer (RT) was patterned on each membrane. Assembling the monolayer flake on the microdevice to bridge the two suspended membranes is one challenge in such measurements. To overcome this, we utilized a technique developed based on a poly(methyl methacrylate) (PMMA) carrier layer[45] for the assembly of a single-walled carbon nanotube network in our previous work.[46] After successful transfer of the flake on the membranes, the sample was immediately loaded into a high-vacuumed cryostat and to perform the thermal transport measurement, one membrane was Joule-heated and part of the heat was conducted through the suspended flake to the other membrane. The temperature rise in the two membranes was measured using the two Pt RTs. From the measured Joule heat and membrane temperatures, we obtained the total thermal resistance of the sample.

RESULTS AND DISCUSSION

A total of two pristine $MoSe_2$ monolayers, denoted as samples 1 and 2, and one doped $Mo_{0.82}W_{0.18}Se_2$ monolayer were successfully assembled on the microdevice using the PMMA transfer process,[45,46] as illustrated in Figure 2a−c, respectively. The through-substrate hole under the two membranes allowed us to conduct transmission electron microscopy (TEM) characterization on the same suspended monolayer used for thermal measurements, which makes the correlation between the measured thermal conductivity and crystal structure information possible. Figure 2d−i shows the low- and high-resolution TEM images of the samples. After the PMMA transfer process, the viscous forces exerted on the assembled sample by the acetone during the drying process caused the samples to deform at the edges (Figure 2g,h). The dimensions and integrity of the sample are validated by the structural characterizations. The existence of PMMA residues reported for the MoS_2,[47] h-BN,[48] and graphene[49] transferred with the same technique was also

DOI: 10.1021/acsami.7b14310
ACS Appl. Mater. Interfaces 2018, 10, 4921−4928

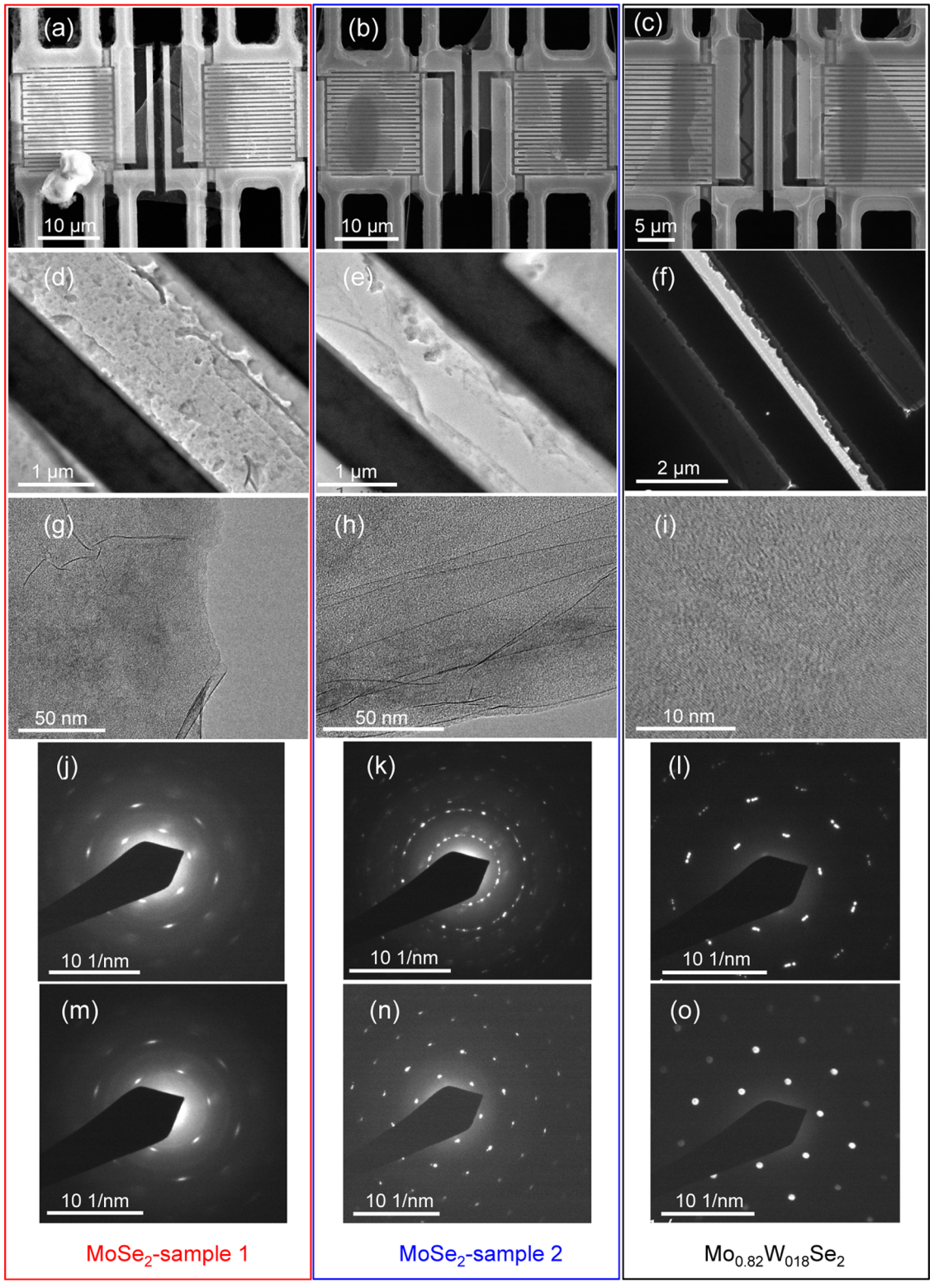

Figure 2. Structural characteristics of the samples. The red, blue, and black boxes contain images for $MoSe_2$-sample 1, $MoSe_2$-sample 2, and $Mo_{0.82}W_{0.18}Se_2$, respectively. (a–c) SEM images, (d–f) low-resolution and (g–i) high-resolution TEM images, (j–l) selected area diffraction patterns of the region close to the edge and (m–o) at the middle of the suspended segment of the samples.

observed on our samples, as seen in Figure 2d,e. Furthermore, an amorphous-like layer was observed in the high-resolution TEM images (Figure 2g–i) that originates from the PMMA residues and the oxidation of the samples, as it is known that the TMDs undergo the aging effect.[50] The selected area electron beam diffraction (SAED) patterns were taken from two different regions on the suspended segment of the samples, one close to the edge (Figure 2j–l) and the other close to the middle part (Figure 2m–o). The SAED patterns close to the edge show more than one set of hexagonal Bragg reflections, which are in contrast

DOI: 10.1021/acsami.7b14310
ACS Appl. Mater. Interfaces 2018, 10, 4921–4928

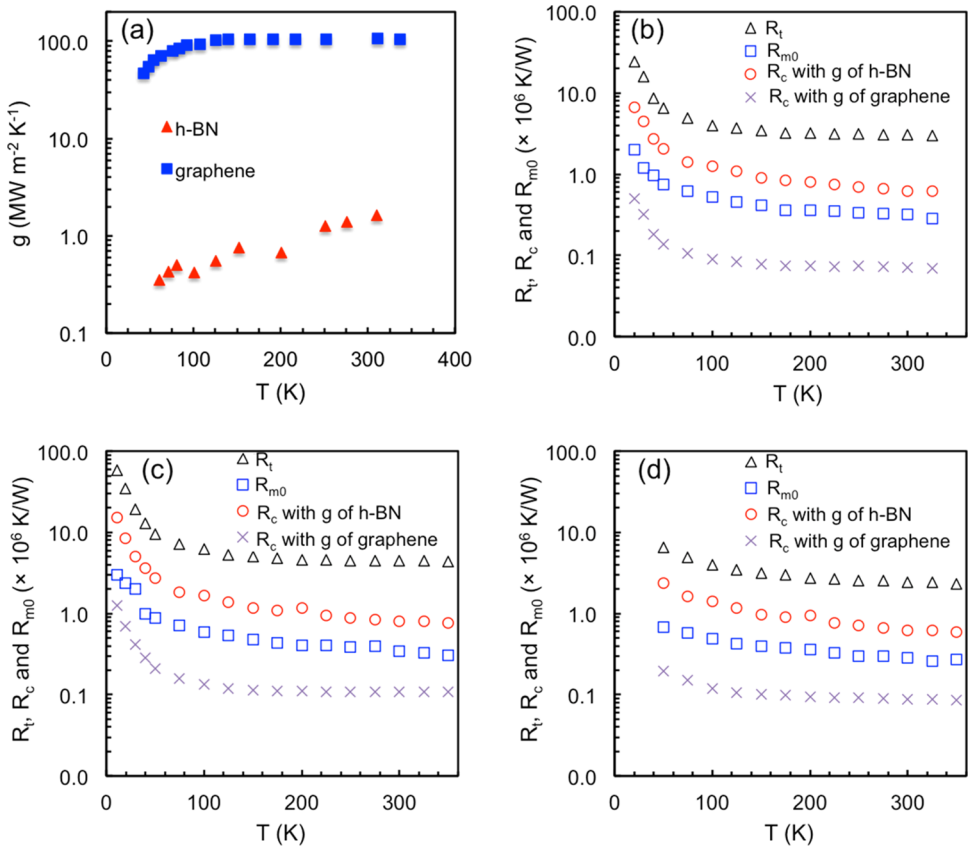

Figure 3. (a) Reported interfacial thermal conductance of few-layer h-BN and few-layer graphene used for calculating the contact thermal resistance. Reprinted in part with permission from ref 48. Copyright 2013 American Chemical Society. Reprinted in part with permission from ref 53. Copyright 2009 American Institute of Physics. (b–d) Total (R_t), internal (R_{m0}), and contact (R_c) thermal resistances of (b) $MoSe_2$ sample 1, (c) $MoSe_2$ sample 2, and (d) $Mo_{0.82}W_{0.18}Se_2$.

to the SAED patterns taken from the middle part of the sample. We believe this discrepancy is because at the edge, the sample is deformed due to the viscous forces acting on the sample upon the acetone drying process. This deformation of the flake at the edge of the sample causes it to fold on top of itself and thus generate more than one set of hexagonal diffraction patterns. On the other hand, the middle part of the sample is intact, hence the one set of hexagonal Bragg reflections that validates the single-crystallinity of our CVD-grown samples.

The measured thermal resistance of the sample (R_t) consists of contributions from (a) the intrinsic thermal resistance of the suspended segment of the flake between the two membranes, (b) the contact thermal resistance between the flake and two membranes (R_c), and (c) the internal thermal resistance of the two membranes caused by the nonuniform temperature distribution on the membranes (R_{m0}). To quantify each component of the measured total thermal resistance, we follow the procedure described in refs 47, 48, and 51 (see details of part I in the Supporting Information). Our calculation is sensitive to the interfacial thermal conductance (g) between the sample and the supporting membranes (Pt/SiN_x in our case). Unfortunately, up to now, there is no reported temperature-dependent interfacial thermal conductance of the $MoSe_2$ monolayer except at room temperature, which was measured on the SiO_2 substrate in ref 37 to be 0.09 ± 0.03 MW m^{-2} K^{-1}. In addition, interfacial thermal conductance of monolayer 2D TMDs is a topic of ongoing research to this date, with reported values that range with orders of magnitude difference. Specifically, the few reported experimental values of interfacial thermal conductance of monolayer MoS_2 at room temperature are g = 1.94, 0.44, and 14 MW m^{-2} K^{-1} in refs 36, 37, and 52, respectively. Because there is no current reliable data for interfacial thermal conductance between monolayer $MoSe_2$ and the Pt/SiN_x of our device, we used the lowest and highest g data of 2D materials in the literature that belong to few-layer h-BN[48] transferred onto suspended Pt/SiN_x devices with a PMMA-assisted technique and few-layer graphene[53] encased in SiO_2, as shown in Figure 3a.

Figure 3b–d shows the R_t, R_{m0}, and R_c calculated with g of h-BN and graphene as a function of temperature for all samples. The R_{m0} and R_c are in agreement with previous results on suspended few-layer graphene[39] and MoS_2.[47] Throughout the whole temperature range, the values of R_{m0} are one order of magnitude smaller than those of R_t. At room temperature, the obtained R_c/R_t ratios for $MoSe_2$ sample 1, sample 2, and $Mo_{0.82}W_{0.18}Se_2$ are, respectively, 20, 18, and 25% if using the few-layer h-BN interfacial conductance and 2.3, 2.4, and 3.6% if using the few-layer graphene interfacial conductance.

The thermal conductivity (κ) was then calculated from the intrinsic thermal resistance for both interfacial thermal conductance of few-layer h-BN and few-layer graphene by taking account of the dimensions of the suspended segment of the sample, as listed in Table 1. Figure 4 shows the intrinsic basal plane thermal conductivities as a function of temperature for all samples measured in this work. The higher g value of graphene compared to that of h-BN results in a well thermally grounded flake to the membranes, smaller thermal contact resistance, and as a consequence, smaller calculated intrinsic thermal conductivities of the samples, as illustrated in Figure 4. For the two

DOI: 10.1021/acsami.7b14310
ACS Appl. Mater. Interfaces 2018, 10, 4921–4928

Table 1. Dimensions of the Suspended Segment of the Samples Measured in This Work

	suspended length (μm)	width (μm)	thickness (nm)
$MoSe_2$ sample 1	0.9 ± 0.1	15.7 ± 0.8	0.7 ± 0.05
$MoSe_2$ sample 2	1.0 ± 0.1	12.7 ± 0.8	0.7 ± 0.05
$Mo_{0.82}W_{0.18}Se_2$	0.6 ± 0.1	17.2 ± 0.8	0.7 ± 0.05

pristine $MoSe_2$ monolayers, in which 4% Se vacancy concentration was observed, κ = 37.4 ± 3.6 and 34.2 ± 3.5 W m^{-1} K^{-1} for g of h-BN and κ = 28.7 ± 3.6 and 28.4 ± 3.5 W m^{-1} K^{-1} for g of graphene at 300 K. At the same temperature, thermal conductivity of the exfoliated $MoSe_2$ monolayer has been measured by the optothermal Raman technique[37] and reported to be 59 ± 18 W m^{-1} K^{-1}. The decrease in κ from the value reported in ref 37 can be attributed to the higher vacancy concentration[24] in our CVD-grown samples compared to their exfoliated counterpart, as will be explained later. Similarly, thermal conductivity of suspended CVD graphene was found to be lower than that in exfoliated samples.[31,54] For the $Mo_{0.82}W_{0.18}Se_2$ monolayer with 2% Se vacancy concentration, κ = 31.2 ± 3.7 W m^{-1} K^{-1} for g of h-BN and κ = 23.2 ± 3.7 W m^{-1} K^{-1} for g of graphene at 300 K. These results indicate that there is an ∼15% reduction in the thermal conductivity due to doping, even though substitutional doping of $MoSe_2$ monolayer by W atoms considerably suppresses the Se vacancy concentration. As will be discussed later, this is not the contributing factor in the thermal conductivity reduction but rather the difference in the sample lengths (1 μm for the pristine vs 0.6 μm for the doped sample). Furthermore, both pristine and W-doped $MoSe_2$ monolayers exhibit a nanostructured behavior at low temperatures, i.e., monotonically increasing thermal conductivity with temperature. This can be understood by the circumstance that the surface scattering dominates over defect and phonon−phonon scattering at these temperatures, as will be elucidated later.

To obtain a deeper insight into the phonon transport processes in our samples and quantitatively interpret the experimental data, we modeled pristine $MoSe_2$ and W-doped $MoSe_2$ ($Mo_{0.82}W_{0.18}Se_2$) with different levels of Se vacancies. Our approach is based on the first-principles density functional theory (DFT) and Boltzmann transport equations (BTEs) (see details of part II in the Supporting Information). Our optimized lattice constant of the monolayer $MoSe_2$ as 3.32 Å agrees well with the experimental value (3.30 Å).[39,55] The iterative solution of the BTE is used to predict the thermal conductivity of $MoSe_2$ and $Mo_{0.82}W_{0.18}Se_2$ using the second-order harmonic and third-order anharmonic interatomic force constants obtained from the DFT calculations. In addition, a model for estimating the effect of defects on phonon properties of the monolayer $MoSe_2$ is developed by incorporating the phonon scattering corresponding to the removal of the mass of atoms and the change of force constants between the under-coordinated atoms near the vacancies (see details in the Supporting Information). In addition, the effect of sample size on the thermal conductivity is also taken into account.

Figure 5a shows that the computed thermal conductivities for the 1 μm long $MoSe_2$ monolayer with 4% Se vacancy concentration and 0.5 μm long $Mo_{0.82}W_{0.18}Se_2$ monolayer with 2% Se vacancy concentration at 300 K are 27.4 and 21.0 W m^{-1} K^{-1}, respectively. They are close to the experimental results, i.e., κ = 28.7 ± 3.6 and 28.4 ± 3.5 W m^{-1} K^{-1} for $MoSe_2$ monolayer and κ = 23.2 ± 3.7 W m^{-1} K^{-1} for the $Mo_{0.82}W_{0.18}Se_2$ monolayer, respectively, calculated on the basis of g of graphene. However, the trend of the thermal conductivity with increasing temperature from our simulations does not match with that from the measurements. First, the temperature corresponding to peak thermal conductivity from the simulations is much lower than that of the experiment. Second, Figure 5a indicates that the thermal conductivity predicted by simulations decreases sharply as the temperature increases, which is due to the dominance of Umklapp scattering at high temperatures. However, in the experiment, the shape of the temperature-dependent thermal conductivity becomes much flatter than that in the simulation as the temperature increases. One reason for the mismatch between the experimental and simulation results is the strong phonon scattering caused by the impurities (residual PMMA and native oxide layers) in the samples considered.[49,56,57] The residual polymer and native oxide layers, as surface disorders, act essentially as a support layer that can suppress the ZA modes in the monolayer $MoSe_2$ and W-doped $MoSe_2$ due to the

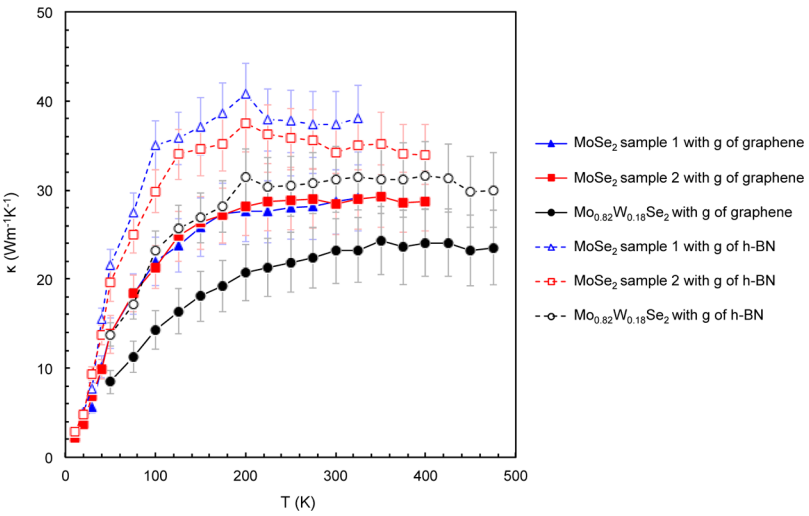

Figure 4. Intrinsic basal plane thermal conductivity of the samples as a function of temperature calculated with g of graphene for $MoSe_2$ sample 1 (filled triangles), $MoSe_2$ sample 2 (filled squares), $Mo_{0.82}W_{0.18}Se_2$ (filled circles), and g of h-BN for $MoSe_2$ sample 1 (unfilled triangles), $MoSe_2$ sample 2 (unfilled squares), and $Mo_{0.82}W_{0.18}Se_2$ (unfilled circles).

DOI: 10.1021/acsami.7b14310
ACS Appl. Mater. Interfaces 2018, 10, 4921−4928

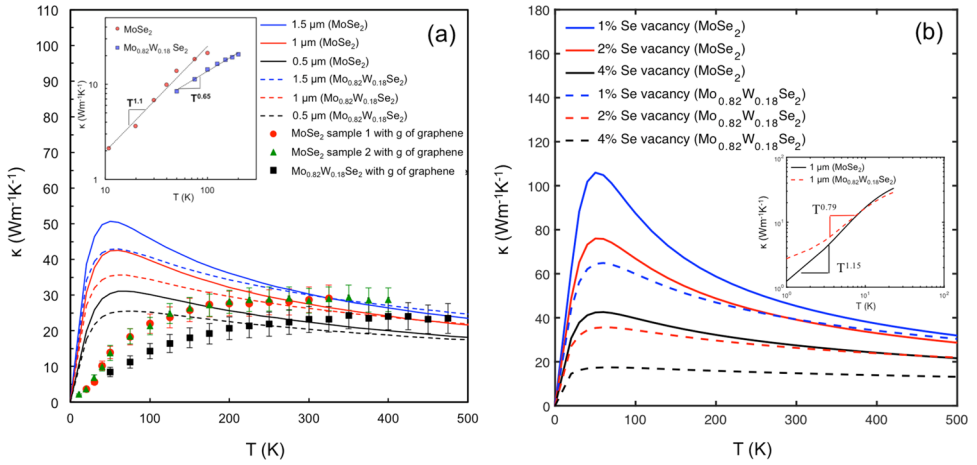

Figure 5. Se vacancy and sample length-dependent thermal conductivity of monolayer $MoSe_2$ and $Mo_{0.82}W_{0.18}Se_2$. (a) The Monolayer $MoSe_2$ with 4% Se vacancy and $Mo_{0.82}W_{0.18}Se_2$ with 2% Se vacancy for different sample lengths. The experimental data processed with *g* of graphene for all samples is also shown. The insert shows the experimentally observed thermal conductivity scaling with temperature at low temperatures. (b) The monolayer $MoSe_2$ with 1, 2, and 4% Se vacancy and $Mo_{0.82}W_{0.18}Se_2$ with 1, 2, and 4% Se vacancy (1 μm sample length). The insert shows the calculated thermal conductivity of the $MoSe_2$ with 4% Se vacancy and $Mo_{0.82}W_{0.18}Se_2$ with 2% Se vacancy scaling, with temperature at low temperatures.

scattering with the support layer (~impurities). This reduces the maximum value of the thermal conductivity and increases the temperature where the peak is located. In addition, the diffuse phonon-surface scattering caused by the residual polymer and native oxide layers is not temperature sensitive, which flattens the thermal conductivity curve at the high temperatures and the sensitivity of the three-phonon process with temperature does not show up in Figure 5b.

The sample size also has a significant influence on the thermal conductivity of the monolayer $MoSe_2$, as shown in Figure 5a. As the length of the sample decreases, the phonon boundary scattering becomes dominant and the phonon−phonon scattering becomes relatively weak, which flattens the temperature-dependent thermal conductivity at high temperature. The size effect can be ignored if the sample size is larger than 10 μm because the maximum phonon mean free path in $MoSe_2$ is around 10 μm.

As illustrated in the insert of Figure 5a, the experimentally observed thermal conductivity for the 1 μm long $MoSe_2$ monolayer with 4% Se vacancy concentration follows $T^{1.1}$ at T < 100 K and that of the 0.6 μm long $Mo_{0.82}W_{0.18}Se_2$ monolayer with 2% Se vacancy concentration follows $T^{0.65}$ at T < 200 K. Theoretical results show temperature dependence as $\approx T^{1.08-1.28}$ at T < 20 K for 0.5−1.5 μm long $MoSe_2$ monolayer samples, considering the effects of boundary and defects scattering. W doping suppresses the temperature dependence to $T^{0.71-0.92}$, which is in good agreement with the experimental observation, $T^{0.65}$. These values are different from those of theoretical three-dimensional (3D) crystals, where at very low temperatures, $\kappa \propto T^3$ due to weak anharmonic phonon scattering and heat capacity $\propto T^3$ due to the linear acoustic phonon dispersion (the Debye model) at low frequencies and the 3D density of states.[58] However, the existence of the quadratic flexure (out-of-plane) phonon modes in 2D materials and the 2D density of states can lead to a different scaling law of thermal conductivity at low temperatures.[38,39,59] A similar trend was also observed in a previous work on monolayer MoS_2, where such a power law was attributed to the contribution of the quadratic phonon branch and the existence of grain boundaries and surface disorders, such as PMMA residue and oxide layers due to sample aging.[60] The structural analysis did not show any evidence of grain boundaries in our samples, but PMMA residue and oxidation due to aging is evident in the TEM characterization that affect the scattering of phonons of varying frequencies.

Furthermore, even though the W doping suppresses the Se-vacant sites by 50% (from 4 to 2%), the thermal conductivity of monolayer $MoSe_2$ and W-doped $MoSe_2$ is still similar in both measurements and simulations. We calculated the thermal conductivities of the pristine $MoSe_2$ and $Mo_{0.82}W_{0.18}Se_2$ monolayer without defects as 55.1 and 51.0 W m^{-1} K^{-1}, respectively. As depicted in Figure 5b, results indicate that the existence of 1, 2, and 4% Se vacancy concentrations decrease the thermal conductivity of the monolayer $MoSe_2$ by 11.2, 23.4, and 46.2%, respectively, at the room temperature, whereas that of the $Mo_{0.82}W_{0.18}Se_2$ monolayer by 27.0, 51.0, and 72.2%, respectively. The W-doped $MoSe_2$ have a stronger sensitivity to the defects than pristine $MoSe_2$. As the mass of the W atom is larger than that of the Mo atom, the missing Se atom at a vacancy site results in the larger mass difference and kinetic energy and potential energy difference. This further enhances the phonon scattering due to the defects and results in the suppression of the thermal conductivity.

CONCLUSIONS

In summary, we report the impact of isoelectronic W doping and Se vacancies on the thermal conductivity of the suspended $MoSe_2$ monolayer grown by CVD. Experimental observations reveal that even though the isoelectronic substitution of the W atoms for Mo atoms in the CVD-grown $Mo_{0.82}W_{018}Se_2$ monolayer reduces the Se vacancy concentration by 50% compared to that found in the $MoSe_2$ monolayer, the thermal conductivity remains almost unchanged in a wide temperature range. This was further confirmed by calculations based on first-principles density functional theory (DFT) and the Boltzmann transport equations (BTEs). However, there is a mismatch between the experimental and simulation results for the trend of temperature dependency of thermal conductivity. This discrepancy is attributed to the strong phonon scattering caused by the residual PMMA and oxide layers on the monolayer flakes that essentially act as a support layer and suppress the ZA mode, which is not fully captured in the calculations. Interestingly, we found that the phonon transport in the W-doped $MoSe_2$ is more

DOI: 10.1021/acsami.7b14310
ACS Appl. Mater. Interfaces 2018, 10, 4921−4928

sensitive to the Se-vacant sites than that in pristine $MoSe_2$ due to the difference in their potential energy. Also, the prominent role of boundary scattering over defects and phonon−phonon scattering at low temperatures for both material systems is evident by the monotonically increasing thermal conductivity with temperature at these temperatures. Overall, these results demonstrate the paramount structure−phonon transport link in 2D TMDs paving the route of their successful integration into modern solid-state devices.

■ ASSOCIATED CONTENT

Supporting Information

The Supporting Information is available free of charge on the ACS Publications website at DOI: 10.1021/acsami.7b14310.

More detailed information about the thermal measurements, COMSOL simulation, DFT and BTE theoretical calculations (PDF)

■ AUTHOR INFORMATION

Corresponding Author

*E-mail: amavrokefalos@uh.edu.

ORCID

Milad Yarali: 0000-0003-1716-8523
Zhequan Yan: 0000-0001-8026-0264
Mina Yoon: 0000-0002-1317-3301
Kai Xiao: 0000-0002-0402-8276
Anastassios Mavrokefalos: 0000-0001-8886-6383

Author Contributions

⊥M.Y. and H.B. contributed equally to this work.

Notes

The authors declare no competing financial interest.

■ ACKNOWLEDGMENTS

A.M. acknowledges financial support from the University of Houston. Synthesis and optical characterization of 2D materials were conducted at the Center for Nanophase Materials Sciences, which is a DOE Office of the Science User Facility. The theoretical calculation was supported by the ORNL Laboratory Directed Research and Development funding. This research used the resources of the National Energy Research Scientific Computing Center, a DOE Office of Science User Facility supported by the Office of Science of the U.S. Department of Energy under the Contract No. DE-AC02-05CH11231.

■ REFERENCES

(1) Mak, K. F.; Lee, C.; Hone, J.; Shan, J.; Heinz, T. F. Atomically Thin MoS_2: A New Direct-Gap Semiconductor. *Phys. Rev. Lett.* **2010**, *105*, No. 136805.

(2) Zhang, Y.; Chang, T.-R.; Zhou, B.; Cui, Y.-T.; Yan, H.; Liu, Z.; Schmitt, F.; Lee, J.; Moore, R.; Chen, Y.; Lin, H.; Jeng, H.-T.; Mo, S.-K.; Hussain, Z.; Bansil, A.; Shen, Z.-X. Direct Observation of the Transition from Indirect to Direct Bandgap in Atomically Thin Epitaxial $MoSe_2$. *Nat. Nanotechnol.* **2014**, *9*, 111−115.

(3) Bernardi, M.; Palummo, M.; Grossman, J. C. Extraordinary Sunlight Absorption and One Nanometer Thick Photovoltaics Using Two-Dimensional Monolayer Materials. *Nano Lett.* **2013**, *13*, 3664−3670.

(4) Gutiérrez, H. R.; Perea-Lopez, N.; Elias, A. L.; Berkdemir, A.; Wang, B.; Lv, R.; Lopez-Urias, F.; Crespi, V. H.; Terrones, H.; Terrones, M. Extraordinary Room-Temperature Photoluminescence in Triangular WS_2 Monolayers. *Nano Lett.* **2013**, *13*, 3447−3454.

(5) Wang, Q. H.; Kalantar-Zadeh, K.; Kis, A.; Coleman, J. N.; Strano, M. S. Electronics and Optoelectronics of Two-Dimensional Transition Metal Dichalcogenides. *Nat. Nanotechnol.* **2012**, *7*, 699−712.

(6) Tongay, S.; Zhou, J.; Ataca, C.; Lo, K.; Matthews, T. S.; Li, J.; Grossman, J. C.; Wu, J. Thermally Driven Crossover from Indirect toward Direct Bandgap in 2D Semiconductors: $MoSe_2$ versus MoS_2. *Nano Lett.* **2012**, *12*, 5576−5580.

(7) Mak, K. F.; He, K.; Shan, J.; Heinz, T. F. Control of Valley Polarization in Monolayer MoS_2 by Optical Helicity. *Nat. Nanotechnol.* **2012**, *7*, 494−498.

(8) Radisavljevic, B.; Radenovic, A.; Brivio, J.; Giacometti, V.; Kis, A. Single-Layer MoS_2 Transistors. *Nat. Nanotechnol.* **2011**, *6*, 147−150.

(9) Buscema, M.; Barkelid, M.; Zwiller, V.; Van Der Zant, H. S. J.; Steele, G. A.; Castellanos-Gomez, A. Large and Tunable Photothermoelectric Effect in Single-Layer MoS_2. *Nano Lett.* **2013**, *13*, 358−363.

(10) Jin, Z.; Liao, Q.; Fang, H.; Liu, Z.; Liu, W.; Ding, Z.; Luo, T.; Yang, N. A Revisit to High Thermoelectric Performance of Single-Layer MoS_2. *Sci. Rep.* **2015**, *5*, No. 18342.

(11) Hippalgaonkar, K.; Wang, Y.; Ye, Y.; Qiu, D. Y.; Zhu, H.; Wang, Y.; Moore, J.; Louie, S. G.; Zhang, X. High Thermoelectric Power Factor in Two-Dimensional Crystals of MoS_2. *Phys. Rev. B* **2017**, *95*, No. 115407.

(12) Lehtinen, O.; Komsa, H.-P.; Pulkin, A.; Whitwick, M. B.; Chen, M.-W.; Lehnert, T.; Mohn, M. J.; Yazyev, O. V.; Kis, A.; Kaiser, U.; Krasheninnikov, A. V. Atomic Scale Microstructure and Properties of Se-Deficient Two-Dimensional $MoSe_2$. *ACS Nano* **2015**, *9*, 3274−3283.

(13) Liu, H.; Zheng, H.; Yang, F.; Jiao, L.; Chen, J.; Ho, W.; Gao, C.; Jia, J.; Xie, M. Line and Point Defects in $MoSe_2$ Bilayer Studied by Scanning Tunneling Microscopy and Spectroscopy. *ACS Nano* **2015**, *9*, 6619−6625.

(14) Li, H.; Tsai, C.; Koh, A. L.; Cai, L.; Contryman, A. W.; Fragapane, A. H.; Zhao, J.; Han, H. S.; Manoharan, H. C.; Abild-Pedersen, F.; Norskov, J. K.; Zheng, X. Activating and Optimizing MoS_2 Basal Planes for Hydrogen Evolution through the Formation of Strained Sulphur Vacancies. *Nat. Mater.* **2016**, *15*, 48−53.

(15) Zan, R.; Ramasse, Q. M.; Jalil, R.; Georgiou, T.; Bangert, U.; Novoselov, K. S. Control of Radiation Damage in MoS_2 by Graphene Encapsulation. *ACS Nano* **2013**, *7*, 10167−10174.

(16) Fu, D.; Zhao, X.; Zhang, Y.-Y.; Li, L.; Xu, H.; Jang, A.-R.; Yoon, S. I.; Song, P.; Poh, S. M.; Ren, T.; Ding, Z.; Fu, W.; Shin, T. J.; Shin, H. S.; Pantelides, S. T.; Zhou, W.; Loh, K. P. Molecular Beam Epitaxy of Highly Crystalline Monolayer Molybdenum Disulfide on Hexagonal Boron Nitride. *J. Am. Chem. Soc.* **2017**, *139*, 9392−9400.

(17) Lee, Y.-H.; Zhang, X.-Q.; Zhang, W.; Chang, M.-T.; Lin, C.-T.; Chang, K.-D.; Yu, Y.-C.; Wang, J. T.-W.; Chang, C.-S.; Li, L.-J.; Lin, T.-W. Synthesis of Large-Area MoS_2 Atomic Layers with Chemical Vapor Deposition. *Adv. Mater.* **2012**, *24*, 2320−2325.

(18) Lin, J.; Pantelides, S. T.; Zhou, W. Vacancy-Induced Formation and Growth of Inversion Domains in Transition-Metal Dichalcogenide Monolayer. *ACS Nano* **2015**, *9*, 5189−5197.

(19) Azizi, A.; Zou, X.; Ercius, P.; Zhang, Z.; Elías, A. L.; Perea-López, N.; Stone, G.; Terrones, M.; Yakobson, B. I.; Alem, N. Dislocation Motion and Grain Boundary Migration in Two-Dimensional Tungsten Disulphide. *Nat. Commun.* **2014**, *5*, No. 4867.

(20) Zhang, K.; Feng, S.; Wang, J.; Azcatl, A.; Lu, N.; Addou, R.; Wang, N.; Zhou, C.; Lerach, J.; Bojan, V.; Kim, M. J.; Chen, L.-Q.; Wallace, R. M.; Terrones, M.; Zhu, J.; Robinson, J. A. Manganese Doping of Monolayer MoS_2: The Substrate Is Critical. *Nano Lett.* **2015**, *15*, 6586−6591.

(21) Gong, Y.; Liu, Z.; Lupini, A. R.; Shi, G.; Lin, J.; Najmaei, S.; Lin, Z.; Laura, A.; Berkdemir, A.; You, G.; Terrones, H.; Terrones, M.; Vajtai, R.; Pantelides, S. T.; Pennycook, S. J.; Lou, J.; Zhou, W.; Ajayan, P. M. Band Gap Engineering and Layer-by-Layer Mapping of Selenium-Doped Molybdenum Disulfide. *Nano Lett.* **2014**, *14*, 442−449.

(22) Mahjouri-Samani, M.; Liang, L.; Oyedele, A.; Kim, Y. S.; Tian, M.; Cross, N.; Wang, K.; Lin, M. W.; Boulesbaa, A.; Rouleau, C. M.; Puretzky, A. A.; Xiao, K.; Yoon, M.; Eres, G.; Duscher, G.; Sumpter, B. G.; Geohegan, D. B. Tailoring Vacancies Far beyond Intrinsic Levels

DOI: 10.1021/acsami.7b14310
ACS Appl. Mater. Interfaces 2018, 10, 4921−4928

Changes the Carrier Type and Optical Response in Monolayer $MoSe_{2-x}$ Crystals. *Nano Lett.* **2016**, *16*, 5213−5220.
(23) Li, X.; Puretzky, A. A.; Sang, X.; Santosh, K. C.; Tian, M.; Ceballos, F.; Mahjouri-Samani, M.; Wang, K.; Unocic, R. R.; Zhao, H.; Duscher, G.; Cooper, V. R.; Rouleau, C. M.; Geohegan, D. B.; Xiao, K. Transition Metal Dichalcogenides: Suppression of Defects and Deep Levels Using Isoelectronic Tungsten Substitution in Monolayer $MoSe_2$. *Adv. Funct. Mater.* **2017**, *27*, No. 1603850.
(24) Lin, Z.; Carvalho, B. R.; Kahn, E.; Lv, R. T.; Rao, R.; Terrones, H.; Pimenta, M. A.; Terrones, M. Defect Engineering of Two-Dimensional Transition Metal Dichalcogenides. *2D Mater.* **2016**, *3*, No. 022002.
(25) Li, X.; Lin, M.-W.; Puretzky, A. A.; Basile, L.; Wang, K.; Idrobo, J. C.; Rouleau, C. M.; Geohegan, D. B.; Xiao, K. Persistent Photoconductivity in Two-Dimensional $Mo_{1-x}W_x Se_2$ −$MoSe_2$ van Der Waals Heterojunctions. *J. Mater. Res.* **2016**, *31*, 923−930.
(26) Li, X.; Lin, M. W.; Basile, L.; Hus, S. M.; Puretzky, A. A.; Lee, J.; Kuo, Y. C.; Chang, L. Y.; Wang, K.; Idrobo, J. C.; Li, A.-P.; Chen, C.-H.; Rouleau, C. M.; Geohegan, D. B.; Xiao, K. Isoelectronic Tungsten Doping in Monolayer $MoSe_2$ for Carrier Type Modulation. *Adv. Mater.* **2016**, *28*, 8240−8247.
(27) Novoselov, K. S.; Geim, A. K.; Morozov, S. V.; Jiang, D.; Katsnelson, M. I.; Grigorieva, I. V.; Dubonos, S. V.; Firsov, A. A. Two-Dimensional Gas of Massless Dirac Fermions in Graphene. *Nature* **2005**, *438*, 197−200.
(28) Novoselov, K. S.; Jiang, D.; Schedin, F.; Booth, T. J.; Khotkevich, V. V.; Morozov, S. V.; Geim, A. K. Two-Dimensional Atomic Crystals. *Proc. Natl. Acad. Sci. U.S.A.* **2005**, *102*, 10451−10453.
(29) Geim, A. K.; Novoselov, K. S. The Rise of Graphene. *Nat. Mater.* **2007**, *6*, 183−191.
(30) Ghosh, S.; Bao, W.; Nika, D. L.; Subrina, S.; Pokatilov, E. P.; Lau, C. N.; Balandin, A. A. Dimensional Crossover of Thermal Transport in Few-Layer Graphene. *Nat. Mater.* **2010**, *9*, 555−558.
(31) Cai, W.; Moore, A. L.; Zhu, Y.; Li, X.; Chen, S.; Shi, L.; Ruoff, R. S. Thermal Transport in Suspended and Supported Monolayer Graphene Grown by Chemical Vapor Deposition. *Nano Lett.* **2010**, *10*, 1645−1651.
(32) Chen, S.; Wu, Q.; Mishra, C.; Kang, J.; Zhang, H.; Cho, K.; Cai, W.; Balandin, A. A.; Ruoff, R. S. Thermal Conductivity of Isotopically Modified Graphene. *Nat. Mater.* **2012**, *11*, 203−207.
(33) Malekpour, H.; Ramnani, P.; Srinivasan, S.; Balasubramanian, G.; Nika, D. L.; Mulchandani, A.; Lake, R. K.; Balandin, A. A. Thermal Conductivity of Graphene with Defects Induced by Electron Beam Irradiation. *Nanoscale* **2016**, *8*, 14608−14616.
(34) Balandin, A. A. Chill out: New Materials and Designs Can Keep Chips Cool. *IEEE Spectrum* **2009**, *46*, 34−39.
(35) Yan, R.; Simpson, J. R.; Bertolazzi, S.; Brivio, J.; Watson, M.; Wu, X.; Kis, A.; Luo, T.; Walker, A. R. H.; Xing, H. G. Thermal Conductivity of Monolayer Molybdenum Disulfide Obtained from Spectroscopy. *ACS Nano* **2014**, *8*, 986−993.
(36) Taube, A.; Judek, J.; Łapińska, A.; Zdrojek, M. Temperature-Dependent Thermal Properties of Supported MoS_2 Monolayers. *ACS Appl. Mater. Interfaces* **2015**, *7*, 5061−5065.
(37) Zhang, X.; Sun, D.; Li, Y.; Lee, G. H.; Cui, X.; Chenet, D.; You, Y.; Heinz, T. F.; Hone, J. C. Measurement of Lateral and Interfacial Thermal Conductivity of Single- and Bilayer MoS_2 and $MoSe_2$ Using Refined Optothermal Raman Technique. *ACS Appl. Mater. Interfaces* **2015**, *7*, 25923−25929.
(38) Li, W.; Carrete, J.; Mingo, N. Thermal Conductivity and Phonon Linewidths of Monolayer MoS_2 from First Principles. *Appl. Phys. Lett.* **2013**, *103*, No. 253103.
(39) Gu, X.; Yang, R. Phonon Transport in Single-Layer Transition Metal Dichalcogenides: A First-Principles Study. *Appl. Phys. Lett.* **2014**, *105*, No. 131903.
(40) Peng, B.; Ning, Z.; Zhang, H.; Shao, H.; Xu, Y.; Ni, G.; Zhu, H. Beyond Perturbation: Role of Vacancy-Induced Localized Phonon States in Thermal Transport of Monolayer MoS_2. *J. Phys. Chem. C* **2016**, *120*, 29324−29331.
(41) Hong, Y.; Zhang, J.; Zeng, X. C. Thermal Conductivity of Monolayer $MoSe_2$ and MoS_2. *J. Phys. Chem. C* **2016**, *120*, 26067−26075.
(42) Ding, Z.; Pei, Q.-X.; Jiang, J.-W.; Zhang, Y.-W. Manipulating the Thermal Conductivity of Monolayer MoS_2 via Lattice Defect and Strain Engineering. *J. Phys. Chem. C* **2015**, *119*, 16358−16365.
(43) Shi, L.; Li, D.; Yu, C.; Jang, W.; Kim, D.; Yao, Z.; Kim, P.; Majumdar, A. Measuring Thermal and Thermoelectric Properties of One-Dimensional Nanostructures Using a Microfabricated Device. *J. Heat Transfer* **2003**, *125*, 881−888.
(44) Mavrokefalos, A.; Pettes, M. T.; Zhou, F.; Shi, L. Four-Probe Measurements of the in-Plane Thermoelectric Properties of Nanofilms. *Rev. Sci. Instrum.* **2007**, *78*, No. 034901.
(45) Suk, J. W.; Kitt, A.; Magnuson, C. W.; Hao, Y.; Ahmed, S.; An, J.; Swan, A. K.; Goldberg, B. B.; Ruoff, R. S. Transfer of CVD-Grown Monolayer Graphene onto Arbitrary Substrates. *ACS Nano* **2011**, *5*, 6916−6924.
(46) Yarali, M.; Hao, J.; Khodadadi, M.; Brahmi, H.; Chen, S.; Hadjiev, V. G.; Jung, Y. J.; Mavrokefalos, A. Physisorbed versus Chemisorbed Oxygen Effect on Thermoelectric Properties of Highly Organized Single Walled Carbon Nanotube Nanofilms. *RSC Adv.* **2017**, *7*, 14078−14087.
(47) Jo, I.; Pettes, M. T.; Ou, E.; Wu, W.; Shi, L. Basal-Plane Thermal Conductivity of Few-Layer Molybdenum Disulfide. *Appl. Phys. Lett.* **2014**, *104*, No. 201902.
(48) Jo, I.; Pettes, M. T.; Kim, J.; Watanabe, K.; Taniguchi, T.; Yao, Z.; Shi, L. Thermal Conductivity and Phonon Transport in Suspended Few-Layer Hexagonal Boron Nitride. *Nano Lett.* **2013**, *13*, 550−554.
(49) Pettes, M. T.; Jo, I.; Yao, Z.; Shi, L. Influence of Polymeric Residue on the Thermal Conductivity of Suspended Bilayer Graphene. *Nano Lett.* **2011**, *11*, 1195−1200.
(50) Gao, J.; Li, B.; Tan, J.; Chow, P.; Lu, T. M.; Koratkar, N. Aging of Transition Metal Dichalcogenide Monolayers. *ACS Nano* **2016**, *10*, 2628−2635.
(51) Wang, J.; Zhu, L.; Chen, J.; Li, B.; Thong, J. T. L. Suppressing Thermal Conductivity of Suspended Tri-Layer Graphene by Gold Deposition. *Adv. Mater.* **2013**, *25*, 6884−6888.
(52) Yalon, E.; McClellan, C. J.; Smithe, K. K. H.; Muñoz Rojo, M.; Xu, R. L.; Suryavanshi, S. V.; Gabourie, A. J.; Neumann, C. M.; Xiong, F.; Farimani, A. B.; Pop, E. Energy Dissipation in Monolayer MoS_2 Electronics. *Nano Lett.* **2017**, *17*, 3429−3433.
(53) Chen, Z.; Jang, W.; Bao, W.; Lau, C. N.; Dames, C. Thermal Contact Resistance between Graphene and Silicon Dioxide. *Appl. Phys. Lett.* **2009**, *95*, No. 161910.
(54) Chen, S.; Moore, A. L.; Cai, W. W.; Suk, J. W.; An, J. H.; Mishra, C.; Amos, C.; Magnuson, C. W.; Kang, J. Y.; Shi, L.; Ruoff, R. S. Raman Measurements of Thermal Transport in Suspended Monolayer Graphene of Variable Sizes in Vacuum and Gaseous Environments. *ACS Nano* **2011**, *5*, 321−328.
(55) Böker, T.; Severin, R.; Müller, A.; Janowitz, C.; Manzke, R.; Voß, D.; Krüger, P.; Mazur, A.; Pollmann, J. Band Structure of MoS_2, $MoSe_2$, and α-$MoTe_2$: Angle-Resolved Photoelectron Spectroscopy and ab initio Calculations. *Phys. Rev. B* **2001**, *64*, No. 235305.
(56) Neogi, S.; Reparaz, J. S.; Pereira, L. F. C.; Graczykowski, B.; Wagner, M. R.; Sledzinska, M.; Shchepetov, A.; Prunnila, M.; Ahopelto, J.; Sotomayor-Torres, C. M.; Donadio, D. Tuning Thermal Transport in Ultrathin Silicon Membranes by Surface Nanoscale Engineering. *ACS Nano* **2015**, *9*, 3820−3828.
(57) Li, G.; Yarali, M.; Cocemasov, A.; Baunack, S.; Nika, D. L.; Fomin, V. M.; Singh, S.; Gemming, T.; Zhu, F.; Mavrokefalos, A.; Schmidt, O. G. In-Plane Thermal Conductivity of Radial and Planar Si/SiO_x Hybrid Nanomembrane Superlattices. *ACS Nano* **2017**, *11*, 8215−8222.
(58) Kittel, C. *Introduction to Solid State Physics*, 7th ed; John Wiley & Sons, Inc: Singapore, 1996.
(59) Wu, X.; Yang, N.; Luo, T. Unusual Isotope Effect on Thermal Transport of Single Layer Molybdenum Disulphide. *Appl. Phys. Lett.* **2015**, *107*, No. 191907.
(60) Yarali, M.; Wu, X.; Gupta, T.; Ghoshal, D.; Xie, L.; Zhu, Z.; Brahmi, H.; Bao, J.; Chen, S.; Luo, T.; Koratkar, N.; Mavrokefalos, A. Effect of Defects on the Temperature-Dependent Thermal Conductivity of Suspended Monolayer Molybdenum Disulfide Grown by Chemical Vapor Deposition. *Adv. Funct. Mater.* **2017**, *27*, No. 1704357.

DOI: 10.1021/acsami.7b14310
ACS Appl. Mater. Interfaces 2018, 10, 4921−4928